Available online at www.sciencedirect.com

ScienceDirect

Green Energy & Environment 11 (2026) 258−268

www.keaipublishing.com/gee

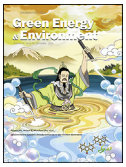

Research Paper

Optimizing CO production in electrocatalytic CO_2 reduction via electron accumulation at Ni sites in $Ni_3ZnC_{0.7}$/Ni on N-doped carbon nanofibers

Min Wang [a,1], Ge Bai [b,c,1], Luwei Peng [d,*], Lulu Li [a], Yadan Yu [a], Wenyi Li [a], Nianjun Yang [e], Daniil I. Kolokolove [f], Jinli Qiao [a,b,c,*]

[a] *State Key Laboratory of Advanced Fiber Materials, College of Environmental Science and Engineering, Donghua University, Shanghai, 201620, China*
[b] *Shanghai Institute of Pollution Control and Ecological Security, Shanghai, 200092, China*
[c] *School of Chemistry and Chemical Engineering, Yancheng Institute of Technology, Yancheng, 224051, China*
[d] *Department of Applied Physics, Hong Kong Polytechnic University, 11 YucaiRoad, Kowloon, Hongkong, China*
[e] *Department of Chemistry & IMO-IMOMEC, Hasselt University, 3590, Diepenbeek, Belgium*
[f] *Boreskov Institute of Catalysis, Siberian Branch of Russian Academy of Sciences, Prospekt Akademika Lavrentieva 5, Novosibirsk, 630090, Russia*

Received 23 February 2025; revised 21 April 2025; accepted 25 April 2025
Available online 29 April 2025

Abstract

The electrocatalytic reduction of carbon dioxide (CO_2RR) to valuable products presents a promising solution for addressing global warming and enhancing renewable energy storage. Herein, we construct a novel $Ni_3ZnC_{0.7}$/Ni heterostructure electrocatalyst, using an electrospinning strategy to prepare metal particles uniformly loaded on nitrogen-doped carbon nanofibers (CNFs). The incorporation of zinc (Zn) into nickel (Ni) catalysts optimizes the adsorption of CO_2 intermediates, balancing the strong binding affinity of Ni with the comparatively weaker affinity of Zn, which mitigates over-activation. The electron transfer within the $Ni_3ZnC_{0.7}$/Ni@CNFs system facilitates rapid electron transfer to CO_2, resulting in great performance with a faradaic efficiency for CO (FE_{CO}) of nearly 90% at −0.86 V versus the reversible hydrogen electrode (RHE) and a current density of 17.51 mA cm^{-2} at −1.16 V versus RHE in an H-cell. Furthermore, the catalyst exhibits remarkable stability, maintaining its crystal structure and morphology after 50 h of electrolysis. Moreover, the $Ni_3ZnC_{0.7}$/Ni@CNFs is used in the membrane electrode assembly reactor (MEA), which can achieve a FE_{CO} of 91.7% at a cell voltage of −3 V and a current density of 200 mA cm^{-2} at −3.9 V, demonstrating its potential for practical applications in CO_2 reduction.

Keywords: CO_2 electroreduction; CO production; $Ni_3ZnC_{0.7}$/Ni; Heterostructure; Membrane electrode assembly

1. Introduction

To address global warming and facilitate renewable energy storage, CO_2RR has emerged as a promising strategy for mitigating CO_2 emissions and converting CO_2 into valuable fuels and chemicals, such as methanol [1,2], carbon monoxide (CO) [3−8], methane [9], formic acid [10−13], ethanol [14], ethylene [15,16], acetic acid [17], and propanol [18]. Among these products, CO is particularly advantageous due to its high economic value, significant selectivity, and ease of separation in liquid electrolytes [19−21]. Furthermore, CO serves as a critical feedstock in tandem reactors for synthesizing multi-

---

* Corresponding authors. State Key Laboratory of Advanced Fiber Materials, College of Environmental Science and Engineering, Donghua University, Shanghai, 201620, China.

E-mail addresses: reedpeng1993@126.com (L. Peng), qiaojl@dhu.edu.cn (J. Qiao).

Peer review under the responsibility of Editorial Board of Green Energy & Environment.

[1] These authors contributed equally to this work.

https://doi.org/10.1016/j.gee.2025.04.010

carbon products or as a component of syngas (CO + H_2), which is essential for producing chemicals like methanol, acetic acid, and dimethyl ether via the Fischer–Tropsch (F-T) process [22–26]. While single-atom catalysts have gained considerable attention for CO_2RR, bimetallic catalysts have demonstrated superior performance due to synergistic effects, tailored coordination environments, and enhanced electron transfer [27–31]. Consequently, the development of cost-effective and efficient bimetallic catalysts for CO_2RR is highly desirable, although elucidating their reaction mechanisms remains a significant challenge.

Among single-atom catalysts, nickel on nitrogen-doped carbon (Ni–N–C) catalysts have shown exceptional promise owing to their large surface area, high electrical conductivity, and tunable structures [32–37]. The coordination-unsaturated and alloyed nickel sites exhibit unique electronic configurations and intermediate adsorption energies, which facilitate the efficient conversion of CO_2 to CO [38–40]. However, the strong affinity of nickel atoms for both carbon and oxygen in CO_2 often leads to the formation of stable bonds, resulting in unstable catalytic activity and poor durability [41]. These limitations hinder the large-scale application of Ni-based catalysts. Generally, the performance of the CO_2RR is fundamentally governed by scaling relationships in the binding energies of reaction intermediates on the catalyst surface. Neither overly strong nor weak binding energies are thermodynamically favourable, necessitating precise modulation of intermediate adsorption strengths at active sites [42]. Bimetallic catalysts offer a promising approach to optimize the binding energies of CO_2 intermediates and modify the electronic structure of the catalyst through strategies such as doping, heterostructure formation, alloying, defect engineering, or surface replacement [43,44].

Recent studies have highlighted the benefits of incorporating Zn into Ni catalysts, as the formation of Ni–Zn metallic bonds or Zn-doped Ni lattices optimizes the adsorption of CO_2 intermediates [45,46]. The strong binding affinity of Ni for carbon and oxygen in CO_2 facilitates effective CO_2 activation, whereas the comparatively weaker affinity of Zn mitigates over-activation, ensuring balanced intermediate adsorption [47]. Specifically, the Ni sites neighboring Zn reduce the energy barriers for CO_2 protonation and subsequent dehydroxylation [48]. For instance, the incorporation of 3% Zn into the Ni lattice modulates the d-band centre through Ni–Zn electronic coupling, balancing the bonding strengths of *COOH and *CO intermediates. This results in a lower energy barrier for CO_2 activation without significant CO poisoning [49]. Moreover, the synergistic interaction between Ni and Zn at binary metal sites promotes *COOH formation, enhancing CO production [50]. Ni–Zn bimetallic sites on nitrogen-doped carbon narrow the gap between the d-band centre of Ni (3d) orbitals and the Fermi energy level, strengthening electronic interactions at the reaction interface [45]. This leads to reduced free energy barriers in the thermodynamic pathway, lower activation energies, and reinforced metal-carbon bonding in the kinetic pathway. For example, a Ni_4N/$Ni_3ZnC_{0.7}$ heterostructure embedded in accordion-like N-doped carbon exhibits a lower energy barrier for *COOH formation compared to individual Ni_4N and $Ni_3ZnC_{0.7}$ phases [51]. The Ni/$Ni_3ZnC_{0.7}$ phase on nitrogen-doped carbon demonstrates strong electron transfer interactions with adsorbed *COOH, outperforming $Ni_3ZnC_{0.7}$-NC and Ni–N–C systems [52,53]. The Ni/$Ni_3ZnC_{0.7}$ phase on nitrogen-doped carbon demonstrates strong electron transfer interactions with adsorbed *COOH, outperforming $Ni_3ZnC_{0.7}$-NC and Ni–N–C systems. These properties accelerate CO_2RR kinetics, improving catalytic activity and selectivity. However, the reaction mechanism of Ni/$Ni_3ZnC_{0.7}$ during CO_2RR remains unclear, and its structural degradation during prolonged stability tests poses a significant challenge.

In this study, we synthesized a $Ni_3ZnC_{0.7}$/Ni heterostructure electrocatalyst supported on porous CNFs via electrospinning. Electron transfer within the $Ni_3ZnC_{0.7}$/Ni@CNFs system occurs from Zn to Ni sites, with electron accumulation at Ni sites facilitating rapid electron transfer to CO_2. This configuration endows the catalyst with superior CO_2 reduction performance, achieving a FE_{CO} of nearly 90% at −0.86 V versus RHE and a current density of 17.51 mA cm^{-2} at −1.16 V versus RHE in an H-cell. The catalyst also demonstrated remarkable stability, with no significant changes in crystal structure and morphology after 50 h of electrolysis. In a MEA setup, the $Ni_3ZnC_{0.7}$/Ni@CNFs catalyst achieved a FE_{CO} of 91.7% at a cell voltage of −3 V and a current density of 200 mA cm^{-2} at −3.9 V, highlighting its potential for practical applications.

2. Experimental

2.1. Materials

Nickel acetate tetrahydrate ($C_4H_{14}NiO_8$, ≥ 99%), Zinc acetate dihydrate ($C_4H_6O_4Zn\cdot 2H_2O$, ≥ 99%), Zinc oxide (ZnO, ≥ 99%), N, N-Dimethylformamide (DMF, ≥ 99.5%) were purchased from Sinopharm Chemical Reagent Co., Ltd. (China). Polyacrylonitrile (PAN, Mw = 150,000) was purchased from Du Pont Co., Ltd. (America). As for electrolytes, potassium bicarbonate ($KHCO_3$, ≥ 99.5%) and potassium hydroxide (KOH, ≥ 99%) were purchased from Sinopharm Chemical Reagent Co., Ltd. (China). Nafion (5wt%), carbon paper, the alkaline anion-exchange membrane of FAB-3-PK-130, and the anion-exchange membrane of Sustainion X37-50 were purchased from Sinero Co., Ltd. (China). All chemicals in this work were analytical grade and employed directly without further purification.

2.2. Synthesis of $Ni_3ZnC_{0.7}$/Ni@CNFs

$Ni_3ZnC_{0.7}$/Ni@CNFs was prepared by the “electrospinning-carbonization” process. In a typical synthesis procedure, PAN (1 g) was first dissolved in DMF (10 mL) at 60 °C with vigorous stirring for 10 h. Next, $C_4H_{14}NiO_8$ (0.6 g), ZnO (0.5 g), and $C_4H_6O_4Zn\cdot 2H_2O$ (0.5 g) were dissolved in the mixed solution at room temperature with vigorously stirring for 12 h to obtain a homogenous mixture for the electrospinning. Subsequently, the mixed solution was loaded into a plastic syringe with a stainless needle at the tip and propelled with a fluid flow rate of 1 mL h^{-1}, and the electrospinning experiment was conducted at a voltage of 20 kV provided by the direct current high-power supply for 10 h. Continuous operation of the dehumidifier is essential during the electrospinning experiment to maintain the relative humidity below 35%, thereby ensuring consistent experimental conditions. The roller collector was fixed 15 cm away from the stainless needle nozzle. After that, the obtained composite nanofiber film was pre-oxidized at low temperature in air (220 °C for 2 h with a heating rate of 1 °C min^{-1}) and then carbonized at high temperature in N_2 (900 °C for 1 h with a heating rate of 5 °C min^{-1}). The dual zinc precursors (ZnO and $C_4H_6O_4Zn \cdot 2H_2O$) enable controlled Zn release during pyrolysis. $C_4H_6O_4Zn \cdot 2H_2O$ decomposes at 200~300 °C to initiate Ni–Zn alloying and carbide formation, while ZnO supplies Zn at > 400 °C to stabilize $Ni_3ZnC_{0.7}$ and prevent Zn loss. In addition, the optimal calcination temperature of 900 °C was selected to balance carbon graphitization and metal stabilization, ensuring sufficient conductivity while preventing metal sintering or excessive carbon loss, as lower temperatures (800 °C) yield incomplete active site formation while higher temperatures (1000 °C) cause detrimental over-graphitization, with 900 °C providing the best catalytic performance through optimal surface area and graphitization degree [54–56]. Finally, the resultant materials were immersed in HCl solution (1.0 mol L^{-1}) for 8 h to remove the remaining Zn species, Ni or NiO nanoparticles. The vivid synthesis process of $Ni_3ZnC_{0.7}$/Ni@CNFs is depicted in Fig. 1a. Ni@CNFs were prepared by a similar procedure without adding ZnO and $C_4H_6O_4Zn \cdot 2H_2O$ acetylacetonate in the mixed solution. Zn@CNFs were synthesized without $C_4H_{14}NiO_8$.

2.3. Materials characterization

Morphologies and structures of these catalysts were observed by scanning electron microscope (SEM, S-4800, 5 kV) and transmission electron microscope (TEM, JEM-2100F, 200 kV). Energy dispersive X-ray spectroscopy (EDS) was carried out at 10 kV to obtain the element distribution. The crystal structures of samples were detected by a Bruker D8 ADVANCE X-ray diffractometer using Cu Kα radiation (l = 1.5406 Å) at 40 kV, 40 mA. The chemical and electronic states of these catalysts were analyzed by X-ray photoelectronic spectroscopy (XPS) which was conducted on Escalab 250Xi equipment. Raman spectra were performed using a Raman spectrometer (in Via-Reflex, λ_{ex} = 532 nm). X-ray absorption fine structure (XAFS) spectra were measured at the

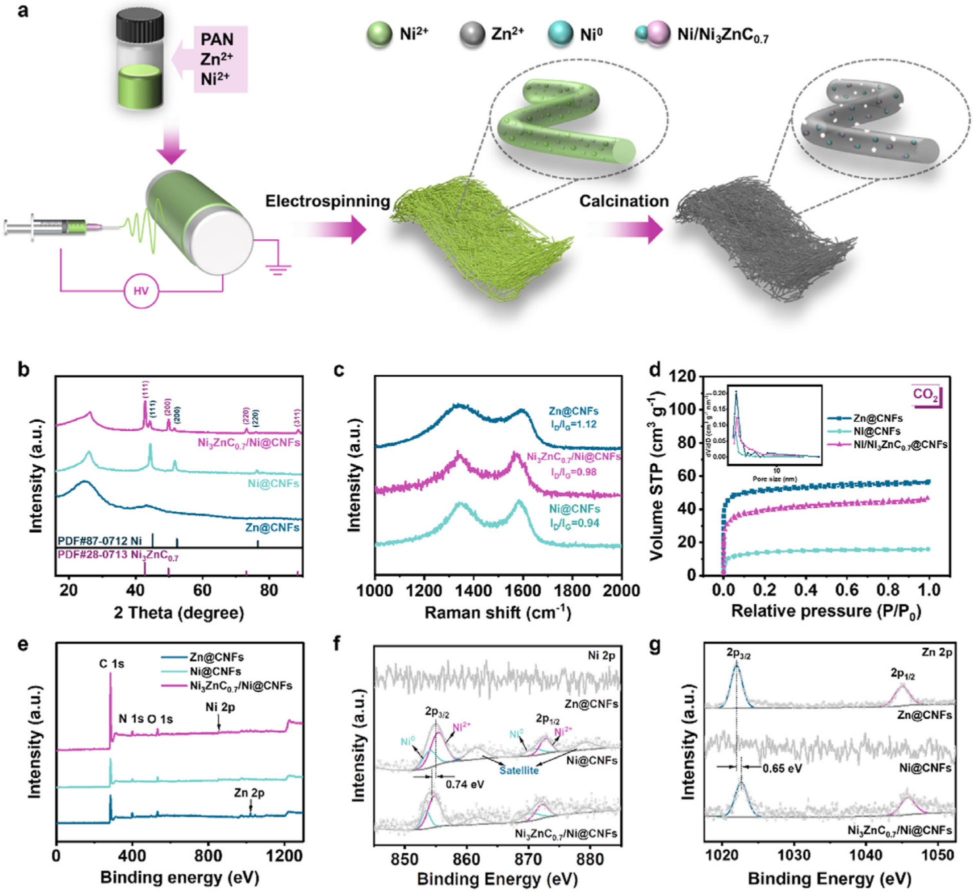

Fig. 1. a) Schematic representation of the synthesis of $Ni_3ZnC_{0.7}$/Ni@CNFs. b) XRD patterns, c) Raman spectra, d) CO_2 Adsorption–desorption isotherm and the pore size distribution of Zn@CNFs, Ni@CNFs, and $Ni_3ZnC_{0.7}$/Ni@CNFs. XPS spectra for e) survey, f) Ni 2p, and g) Zn 2p of Zn@CNFs, Ni@CNFs, and $Ni_3ZnC_{0.7}$/Ni@CNFs.

BL14 beam line platform of the Shanghai Synchrotron Radiation Facility in a transmission mode using an ionization chamber. Ni foil, NiO, NiPc, Ni_2O_3, Zn foil, ZnO, ZnPc, and $ZnCl_2$ were tested as references. The Brunauer–Emmett–Teller (BET) method was employed for studying the specific surface area and porosity of catalysts using CO_2 gas for adsorption and desorption isotherms.

2.4. Electrochemical performance of CO_2 reduction

The preliminary performance tests of the electrochemical CO_2RR of the as-prepared samples were carried out by a workstation (CHI 760E, Shanghai Chenhua) in a two-compartment three-electrode H-type cell, where the anodic and cathodic compartments were separated by an alkaline anion-exchange membrane of FAB-3-PK-130. The H-type cell with the 0.5 mol L^{-1} KOH (30 mL) as anolyte and Pt plate as anode in the anodic compartment, and 0.5 mol L^{-1} $KHCO_3$ (30 mL) as catholyte and an Ag/AgCl electrode as the reference electrode in the cathodic compartment. The working electrode was prepared by spraying it on one side of carbon paper (1×1.5 cm^2). In this study, the optimal catalyst loading for the working electrode was determined to be 1 mg cm^{-2}. While increasing the $Ni_3ZnC_{0.7}$/Ni@CNFs loading to 2 mg cm^{-2} yielded a marginal increase in current density, the CO_2 reduction performance remained comparable, even with a slight decrease in FE_{CO} (86.17% at 1 mg cm^{-2}, 85.38% at 2 mg cm^{-2}), as shown in Fig. S1. Given the negligible performance enhancement and the practical advantages of minimizing catalyst usage, 1 mg cm^{-2} was selected for subsequent experiments. Before the CO_2RR experiment, N_2 and CO_2 gas were respectively bubbled into the catholyte for 30 min to form N_2 and CO_2 saturated electrolyte, and the pH of N_2 and CO_2-saturated 0.5 mol L^{-1} $KHCO_3$ aqueous solutions is 8.43 and 7.48. All the mentioned potentials in this work were converted to the RHE as follows:

$$E_{RHE} = E_{Ag/AgCl} + 0.197 + 0.0591 \times pH \qquad (1)$$

To further improve the reaction rate of CO_2RR, the $Ni_3ZnC_{0.7}$/Ni@CNFs with the excellent performance of CO_2RR selected in the H-type cell was further tested in the MEA set-up. The MEA cell consists of a cathode and an anode chamber separated by a zero-gap membrane electrode, which is made by the cathode of the catalyst-loaded carbon paper (3×3 cm^2, 1 mg cm^{-2}), anion exchange membrane of Sustainion X37-50, and anode of IrO_2@Ti felt (3×3 cm^2, 1 mg cm^{-2}). The bipolar plates of the MEA cell were configured with a single serpentine channel, and the active area of the electrodes was 2×2 cm^2. Humidified CO_2 was inlet in the cathode, and 0.5 mol L^{-1} $KHCO_3$ was used as anolyte. The CO_2 electrolysis was performed under a two-electrode system without any reference electrode. The catalyst inks for the cathode and anode were sprayed on the side of carbon paper and Ti felt facing the Sustainion X37-50 membrane. During the CO_2 electrolysis, the humidified CO_2 was continuously introduced into the cathode chamber, while the anode was circulated 0.5 mol L^{-1} $KHCO_3$ at a flow rate of 30 mL min^{-1} using a peristaltic pump. All performance tests of the electrochemical CO_2RR of the MEA set-up were carried out by a workstation equipped with current amplifier (CHI 760E, Shanghai Chenhua).

2.5. Product analysis

The gas products were analyzed by online gas chromatography (GC9790P, FULI INSTRUMENTS) with a thermal conductivity detector (TCD) and flame ionization detector (FID). The mixture gas of H_2 (100 ppm), CO (102 ppm), C_2H_4 (102 ppm), CH_4 (101 ppm), C_2H_6 (101 ppm), C_2H_2 (101 ppm), and the remaining gas (N_2) as standard gas is used for quantification. The Faradaic efficiency (FE) of CO, H_2, C_2H_4, CH_4, C_2H_2, and C_2H_6 was calculated using the following equation:

$$FE_{gas}(\%) = \frac{\frac{v}{60\ s/min} \times \frac{c}{24000\frac{cm^3}{mol}} \times N \times F}{j_{total}} = \frac{0.067 \times v \times c \times N}{j_{total}} \qquad (2)$$

Where ν is the CO_2 flow rate, and *c* indicates the volume concentration of different gas outlets of the H-cell. *N* denotes the number of electrons transferred to one CO_2 molecule to CO, H_2, C_2H_4, CH_4, C_2H_2, and C_2H_6, and j_{total} refers to the total current density.

3. Physical and chemical characterization

The XRD patterns of Zn@CNFs, Ni@CNFs, and $Ni_3ZnC_{0.7}$/Ni@CNFs are presented in Fig. 1b. The Zn@CNFs exhibit a crystal structure identical to that of pure polyacrylonitrile (PAN) fibers, as shown in Fig. S2a, which is attributed to the volatilization loss of Zn during the calcination and pickling process. In contrast, the Ni@CNFs display three distinct peaks at 44.39°, 51.69°, and 76.27°, corresponding to the (111), (200), and (220) planes of metallic Ni (PDF #87-0712), respectively. This observation confirms the formation of metallic Ni within the Ni@CNFs under N_2 conditions rather than other nickel species. Furthermore, the introduction of ZnO and $C_4H_6O_4Zn \cdot 2H_2O$ prior to electrospinning results in the formation of $Ni_3ZnC_{0.7}$ with (111), (200), and (220) crystal planes at 42.78°, 49.78°, and 73.14° in the $Ni_3ZnC_{0.7}$/Ni@CNFs. The absence of Zn species in pure Zn@CNFs suggests that the co-presence of Ni and Zn species in the precursor mitigates Zn loss by forming Ni–Zn and Zn–N bonds. Consequently, the binary phases of metallic Ni and $Ni_3ZnC_{0.7}$, with abundant grain boundaries and heterojunctions in $Ni_3ZnC_{0.7}$/Ni@CNFs, potentially offer more active sites for electrocatalytic CO_2 reduction compared to Zn@CNFs and Ni@CNFs. The content of metallic Ni and $Ni_3ZnC_{0.7}$ phases can be readily adjusted by varying the ratio of Ni and Zn species in the precursor, as depicted in Fig. S2b. Notably, the $Ni_3ZnC_{0.7}$ phase becomes more pronounced with increased introduction of $C_4H_{14}NiO_8$, indicating that the $Ni_3ZnC_{0.7}$ phase is prone to be formed under Ni-rich conditions.

SEM images of Zn@CNFs, Ni@CNFs, and $Ni_3ZnC_{0.7}$/Ni@CNFs in Fig. S3 reveal a well-defined fibrous structure with diameters ranging from 80 to 120 nm. The carbon fibers exhibit a smooth and clean surface when a small quantity of Ni and Zn sources is used. It was demonstrated that the Zn in single-layer NiZn layered double hydroxides could avoid the agglomeration of Ni atoms during calcining [57]. However, with an excess of Ni and Zn sources, metallic Ni and $Ni_3ZnC_{0.7}$ tend to aggregate and cover the surface of the carbon fibers. Additional structural information is obtained from Raman spectroscopy, which shows two prominent peaks at approximately 1338 cm^{-1} and 1591 cm^{-1}, corresponding to the D and G bands, respectively, as illustrated in Fig. 1c. The D peak indicates lattice defects in the carbon, while the G peak reflects the degree of carbonization [58]. The intensity ratios (I_D/I_G) for Zn@CNFs and $Ni_3ZnC_{0.7}$/Ni@CNFs are 1.12 and 0.98, respectively, suggesting that Zn@CNFs possess more carbon defects than $Ni_3ZnC_{0.7}$/Ni@CNFs. The incorporation of a Ni source in the precursor reduces Zn volatilization by forming bonds with Zn, thereby decreasing carbon defects in the carbon fibers. Meanwhile, the I_D/I_G ratios for Ni@CNFs and $Ni_3ZnC_{0.7}$/Ni@CNFs are 0.98 and 0.94, respectively, indicating a higher degree of carbonization in Ni@CNFs compared to $Ni_3ZnC_{0.7}$/Ni@CNFs. Ni nanoparticles are considered highly effective catalysts for carbon nanotube formation, which may enhance the degree of carbonization relative to Ni/$Ni_3ZnC_{0.7}$ under identical pyrolysis conditions [59].

The CO_2 adsorption–desorption analysis was performed to assess the surface area and porous structure of Zn@CNFs, Ni@CNFs, and $Ni_3ZnC_{0.7}$/Ni@CNFs, as depicted in Fig. 1d. The specific surface area of Zn@CNFs is 52.6 m^2 g^{-1} which is higher than that of Ni@CNFs (19.3 m^2 g^{-1}) and $Ni_3ZnC_{0.7}$/Ni@CNFs (39.0 m^2 g^{-1}), attributed to the evaporation of Zn during the pyrolysis process. Regarding the porous structure, as shown in the inset of Fig. 1d, a prominent peak at approximately 1.8 nm indicates a significant presence of micropores and mesopores. These pores can confine CO_2 molecules and the reaction intermediate (*COOH), facilitating the CO_2 conversion into CO due to the suitable molecular diameter of CO_2 (0.35–0.51 nm). The elemental composition and chemical states of the three samples were examined using XPS, as illustrated in Fig. 1e. Elements C, N, and O can be easily found in all three samples, while Zn and Ni are present in Zn@CNFs and Ni@CNFs, respectively. The XPS spectra of C1s and N1s are shown in Fig. S4. The appearance of C-M bonds in C 1s and the five nitrogen species of pyridinic-N, metal-N, pyrrolic-N, graphitic-N, and oxidized-N in N 1s indicate that elemental N was successfully doped into carbon nanofibers of the three materials. The atomic ratio of Ni to Zn remains unchanged across different samples, as shown in Figs. S5–6, suggesting that Ni is very easily bonded with Zn. The high-resolution Ni 2p spectra of Ni@CNFs and $Ni_3ZnC_{0.7}$/Ni@CNFs exhibit two peaks at 855.1 eV (Ni $2p_{3/2}$) and 872.8 eV (Ni $2p_{1/2}$), which can be deconvoluted into peaks corresponding to Ni^0 and Ni^{2+}, as shown in Fig. 1f. The coexistence of Ni^0 and Ni^{2+} in $Ni_3ZnC_{0.7}$/Ni@CNFs is consistent with the XRD analysis. Notably, the Ni $2p_{3/2}$ peak of $Ni_3ZnC_{0.7}$/Ni@CNFs shows a negative shift of 0.74 eV compared to that of Ni@CNFs, indicating that the Ni site acts as an electron acceptor due to the introduction of Zn. Meanwhile, the high-resolution Zn 2p spectra of Zn@CNFs and $Ni_3ZnC_{0.7}$/Ni@CNFs display two peaks at 1021.9 eV (Zn $2p_{3/2}$) and 1044.9 eV (Zn $2p_{1/2}$) in Fig. 1g, with the Zn $2p_{3/2}$ peak of $Ni_3ZnC_{0.7}$/Ni@CNFs exhibiting a positive shift of 0.65 eV relative to Zn@CNFs, suggesting that the Zn site functions as an electron donor. Consequently, electron transfer in $Ni_3ZnC_{0.7}$/Ni@CNFs occurs from Zn to Ni sites [60]. The accumulation of electrons at Ni sites is advantageous for CO_2 reduction due to the rapid electron transfer from Ni sites to CO_2.

The chemical state, local structures, and coordination environment of $Ni_3ZnC_{0.7}$/Ni@CNFs were examined using X-ray absorption spectroscopy (XAS) [61,62]. As depicted in Fig. 2a, the Ni K-edge X-ray absorption near-edge structure (XANES) spectrum of $Ni_3ZnC_{0.7}$/Ni@CNFs closely resembles that of a reference Ni foil, confirming the presence of Ni^0 or an alloy with other metals, consistent with the XRD analysis results shown in Fig. 1b. The Ni chemical state in $Ni_3ZnC_{0.7}$/Ni@CNFs, as indicated by the oxygen state in Fig. 2b, is 0.09, which is very close to that of Ni^0 in the Ni foil. Additionally, the white line peak height of $Ni_3ZnC_{0.7}$/Ni@CNFs is lower than that of the Ni foil, as shown in the inset of Fig. 2a. These findings suggest that Ni in the Ni–Zn intermetallic phase carries a slightly negative charge compared to Ni in the Ni foil, attributed to electron transfer from Zn to Ni [45], as confirmed by XPS analysis. In Fig. 2c, the Ni foil exhibits three main peaks at 2.18, 4.02, and 4.69 Å, corresponding to Ni–Ni bonds, while the NiO sample shows two main peaks at 1.65 and 2.57 Å, assigned to Ni–O and Ni–Ni bonds. The $Ni_3ZnC_{0.7}$/Ni@CNFs display similar peaks to the Ni foil, with the highest Ni–Ni peak at 2.12 Å showing a negative shift of 0.06 Å, indicating a shortened Ni–Ni bond length due to the formation of Ni–Zn bonds at 3.93 and 4.57 Å. Furthermore, the absence of the Ni–O peak at 1.65 Å in $Ni_3ZnC_{0.7}$/Ni@CNFs suggests the absence of oxygen in the nearest Ni neighbors. The EXAFS spectrum of $Ni_3ZnC_{0.7}$/Ni@CNFs in Figs. S7–8 can be accurately fitted using only the Ni-M (metal) path, confirming the presence of metallic Ni and $Ni_3ZnC_{0.7}$ species. The Zn K-edge XANES spectrum of $Ni_3ZnC_{0.7}$/Ni@CNFs in Fig. 2d shows a higher onset of the absorption edge and a reduced white line peak height compared to Zn foil, indicating that the overall valence of Zn species in $Ni_3ZnC_{0.7}$/Ni@CNFs is close to Zn^0, corroborated by the oxygen state in Fig. 2e. The EXAFS fitting curves in R-space for $Ni_3ZnC_{0.7}$/Ni@CNFs reveal two strong peaks at 1.53 and 2.27 Å, attributed to Zn–N and Zn–Ni/Zn bonds in Fig. 2f. The local structures of the absorbing Ni atoms in $Ni_3ZnC_{0.7}$/Ni@CNFs are further elucidated through wavelet transform (WT) representations of the Ni K-edge EXAFS signals in Fig. 2g–i, showing a spectrum very similar to the theoretical Ni foil model. The Ni–Ni/Zn bond distance in $Ni_3ZnC_{0.7}$/Ni@CNFs exhibits a negative shift compared to the Ni–Ni bond in Ni foil. The Ni–Zn paths in the Zn K-edge WT-EXAFS are as distinct as those in the Ni K-edge WT-EXAFS, with the Zn–N/C path also appearing in Fig. 2j–k. The observed intensity maxima of the Ni–Ni/Zn path at ~8.0 $Å^{-1}$ in Fig. 2g and j for $Ni_3ZnC_{0.7}$/Ni@CNFs closely resemble

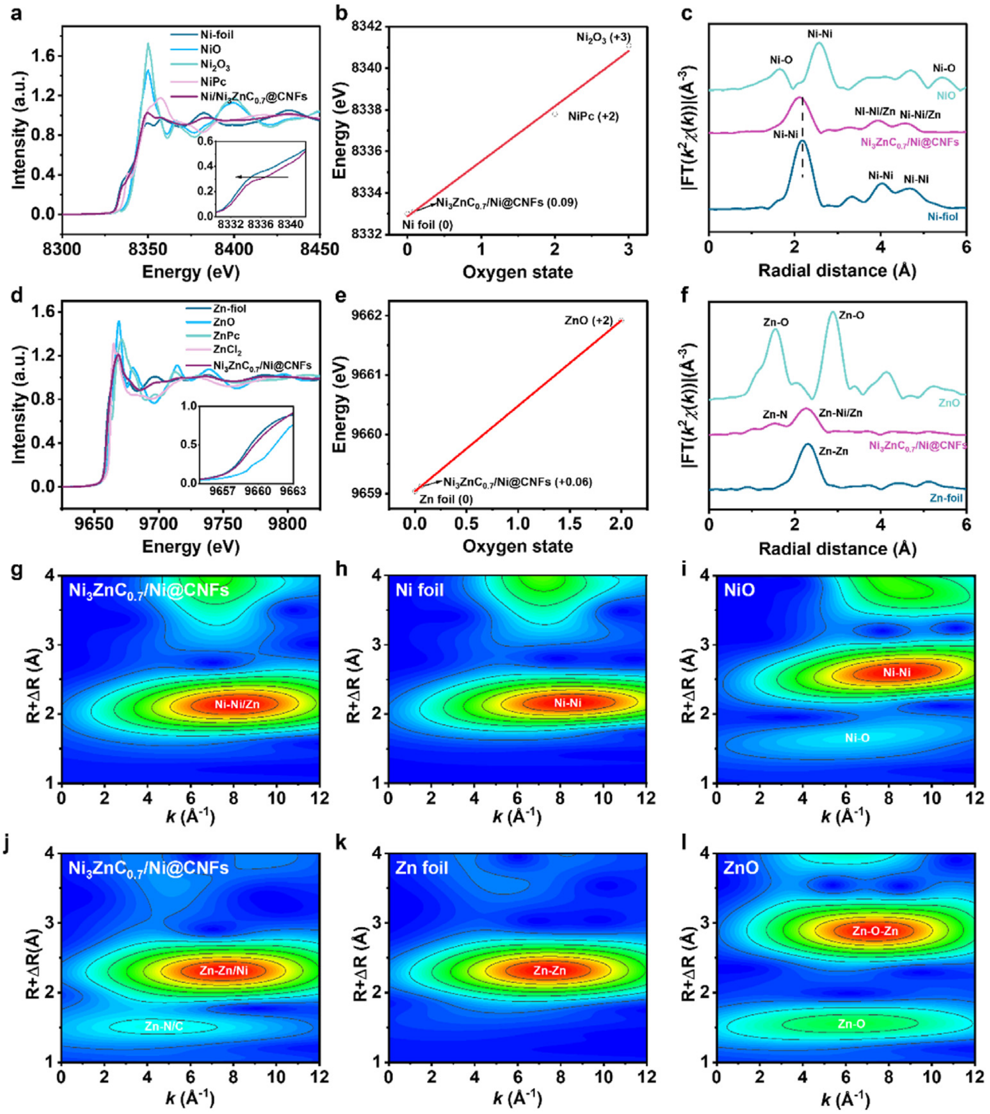

Fig. 2. a) Ni K-edge XANES spectra. b) Ni K-edge XANES fitted curve correlating the average oxygen state of $Ni_3ZnC_{0.7}$/Ni@CNFs, Ni foil, NiPc, and Ni_2O_3. c) Ni K-edge FT-EXAFS spectra in the R-space. d) Zn K-edge XANES spectra. e) Zn K-edge XANES fitted curve correlating the average oxygen state of $Ni_3ZnC_{0.7}$/Ni@CNFs, Zn foil, and ZnO. f) Zn K-edge FT-EXAFS spectra in the R-space. g-i) WT-EXAFS of the Ni K-edge signal for $Ni_3ZnC_{0.7}$/Ni@CNFs, Ni foil, and NiO. j-l) WT-EXAFS of the Zn K-edge signal for $Ni_3ZnC_{0.7}$/Ni@CNFs, Zn foil, and ZnO.

those for Ni foil and differ from those for NiO and ZnO in Fig. 2i and l, further confirming the electronic interaction between Ni and Zn. The EXAFS fitting curves in R-space and k-space align with both the Ni and Zn experimental spectra of $Ni_3ZnC_{0.7}$/Ni@CNFs, as shown in Figs. S7–10. The coordination numbers (CNs), bond distances (R), and Debye-Waller factors (σ^2) are detailed in Tables S1–2.

4. Electrochemical performance

The catalytic performance of Zn@CNFs, Ni@CNFs, and $Ni_3ZnC_{0.7}$/Ni@CNFs for CO_2RR is assessed in Fig. 3a. The LSV polarization curve for $Ni_3ZnC_{0.7}$/Ni@CNFs under CO_2-saturated conditions exhibits a higher current density compared to N_2-saturated conditions, indicating significant activity for CO_2 reduction. At −1.16 V versus RHE, the current density of $Ni_3ZnC_{0.7}$/Ni@CNFs reaches 17.51 mA cm^{-2}, surpassing that of Zn@CNFs (13.24 mA cm^{-2}) and Ni@CNFs (7.97 mA cm^{-2}). The onset potential for $Ni_3ZnC_{0.7}$/Ni@CNFs at 2 mA cm^{-2} is −0.68 V versus RHE, which is lower than that of Zn@CNFs (−0.77 V vs. RHE) and Ni@CNFs (−0.83 V vs. RHE). This lower onset potential and higher current density at the same applied potential underscore the superior CO_2 reduction activity of $Ni_3ZnC_{0.7}$/Ni@CNFs compared to Zn@CNFs and Ni@CNFs. As illustrated in Fig. 3b, the FE_{CO} of $Ni_3ZnC_{0.7}$/Ni@CNFs increases from 36.9% to nearly 90% within the potential range of −0.56 to −0.76 V versus RHE and then decreases between −0.76 and −1.16 V versus RHE. H_2 and CO are the predominant products for $Ni_3ZnC_{0.7}$/Ni@CNFs during CO_2RR. Long-term test analysis revealed no detectable liquid products by NMR spectroscopy, with only negligible trace amounts of formic acid identified through HPLC, as shown in Figs. S11 and S12. The decrease in FE_{CO} at higher potentials is

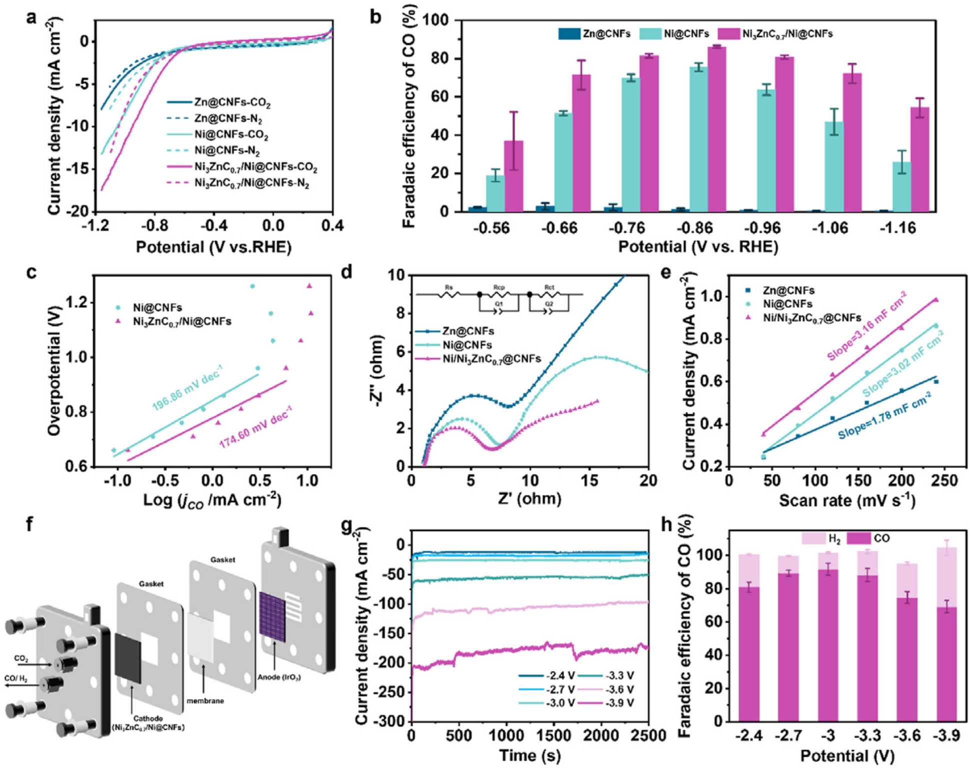

Fig. 3. a) LSV in N_2 and CO_2-saturated 0.5 mol L^{-1} $KHCO_3$ solution at 5 mV s^{-1} scan rate. b) FE_{CO} under different potentials of Zn@CNFs, Ni@CNFs and $Ni_3ZnC_{0.7}$/Ni@CNFs. c) Tafel plots of Ni@CNFs and $Ni_3ZnC_{0.7}$/Ni@CNFs. d) Electrochemical Impedance Spectroscopy (EIS). e) Electrochemical double layer capacitance measurements of Zn@CNFs, Ni@CNFs and $Ni_3ZnC_{0.7}$/Ni@CNFs. f) Schematic diagram of zero-gap membrane electrode cell. g) Current density of $Ni_3ZnC_{0.7}$/Ni@CNFs electrode at different applied potential by i-t curve in zero-gap membrane electrode cell. h) Faradaic efficiency of CO by using $Ni_3ZnC_{0.7}$/Ni@CNFs electrode in zero-gap membrane electrode cell.

attributed to the rapid consumption of CO_2, which is limited by mass transport, thereby favoring the HER. Additionally, the FE_{CO} of Ni@CNFs follows a similar trend to that of $Ni_3ZnC_{0.7}$/Ni@CNFs, with a maximum value not exceeding 80% at all applied potentials, suggesting that the binary phases of metallic Ni and $Ni_3ZnC_{0.7}$, with their abundant grain boundaries and heterojunctions, enhance CO_2RR performance. Notably, the $Ni_3ZnC_{0.7}$/Ni@CNFs catalyst still maintained 79.17% FE_{CO} at −0.86 V versus RHE in a neutral electrolyte (0.5 mol L^{-1} K_2SO_4), as shown in Fig. S13. In contrast, Zn@CNFs exhibit negligible CO_2 reduction activity due to Zn volatilization during the calcination process in Fig. 3a and Fig. S14. The calcination temperature of 900 °C is near the volatilization point of metallic Zn, leading to Zn loss and the absence of active sites for CO_2 reduction. When Zn and Ni sources coexist in the precursor, Ni can form strong bonds with Zn, resulting in the formation of $Ni_3ZnC_{0.7}$ and preventing Zn loss, as demonstrated by the XRD and XAS analyses.

To elucidate the step that plays a critical role in CO generation, the Tafel slopes of Ni@CNFs and $Ni_3ZnC_{0.7}$/Ni@CNFs are presented in Fig. 3c. The Tafel slope for $Ni_3ZnC_{0.7}$/Ni@CNFs is 174.6 mV dec^{-1}, indicating that the chemical rate-determining step for CO generation is the initial electron transfer leading to the formation of the COOH* intermediate. A smaller Tafel slope value suggests a lower overpotential in an electrocatalytic reaction. Thus, the slope of 174.6 mV dec^{-1} for $Ni_3ZnC_{0.7}$/Ni@CNFs, compared to 196.9 mV dec^{-1} for Ni@CNFs, implies that the incorporation of Zn into $Ni_3ZnC_{0.7}$ enhances charge transfer from $Ni_3ZnC_{0.7}$/Ni@CNFs to the adsorbed CO_2* species. This phenomenon is attributed to electron transfer from Zn to Ni, as evidenced by the XPS and XAS analyses. This electron transfer renders Zn electron deficient. The d-band center of $Ni_3ZnC_{0.7}$ is positioned further from the Fermi level compared to pure Ni, resulting in weaker bonding of adsorbates with the metal surface due to the increased filling of antibonding states. Ni atoms exhibit a strong affinity for both carbon and oxygen atoms, forming bonds with them. However, the strong binding of CO on Ni atoms can poison the metal surface, making CO desorption challenging [49]. Yingying Lu et al. reported that Ni/Zn diatoms can significantly reduce the free energy for the *COOH reaction and increase the free energy of *CO compared to Ni atoms [45]. Zn atoms assist Ni in weakening the bonding strength and COOH adsorption, facilitating CO desorption from Ni atoms while also inhibiting the competitive HER. These findings demonstrate that Ni atoms in $Ni_3ZnC_{0.7}$ can be further activated by Zn atoms due to electron transfer from Zn to Ni, leading to electron accumulation at Ni atoms. This enhances the formation of the *COOH intermediate and promotes CO generation.

To further elucidate this electron transfer, electrochemical impedance spectroscopy (EIS) was employed to investigate the charge transfer resistance. The EIS data are fitted using the equivalent circuit depicted in the inset of Fig. 3d, which comprises a series resistance R_S (associated with electrolyte resistance), a parallel combination of the resistance R_{CP} (related to charge transport resistance within the electrocatalyst) and the constant phase element Q_1, and another parallel combination of the resistance R_{CT} (related to charge transfer resistance from the electrocatalyst to the reactant) and the constant phase element Q_2 [10,53,63]. The simulated data in Table S3 confirms that the R_S values for Ni@CNFs, Zn@CNFs, and $Ni_3ZnC_{0.7}$/Ni@CNFs are similar, whereas the R_{CP} and R_{CT} values for $Ni_3ZnC_{0.7}$/Ni@CNFs are slightly lower than those for Ni@CNFs and significantly lower than those for Zn@CNFs. Consequently, the specific charge transfer rate in $Ni_3ZnC_{0.7}$/Ni@CNFs is higher than in Ni@CNFs and Zn@CNFs, and the Zn modification in $Ni_3ZnC_{0.7}$ effectively suppresses the HER. Fig. 3e and Fig. S15 illustrate the slope of the double-layer current against the corresponding scan rate, which reflects the electrochemically active surface area (ECSA). The double-layer capacitance (Cdl) is 3.16 mF cm^{-2} for $Ni_3ZnC_{0.7}$/Ni@CNFs, higher than 3.02 mF cm^{-2} for Ni@CNFs and 1.78 mF cm^{-2} for Zn@CNFs. This indicates that the binary phases of metallic Ni and $Ni_3ZnC_{0.7}$, with their abundant grain boundaries and heterojunctions in $Ni_3ZnC_{0.7}$/Ni@CNFs, provide more active sites than Zn@CNFs and Ni@CNFs for electrocatalytic CO_2 reduction.

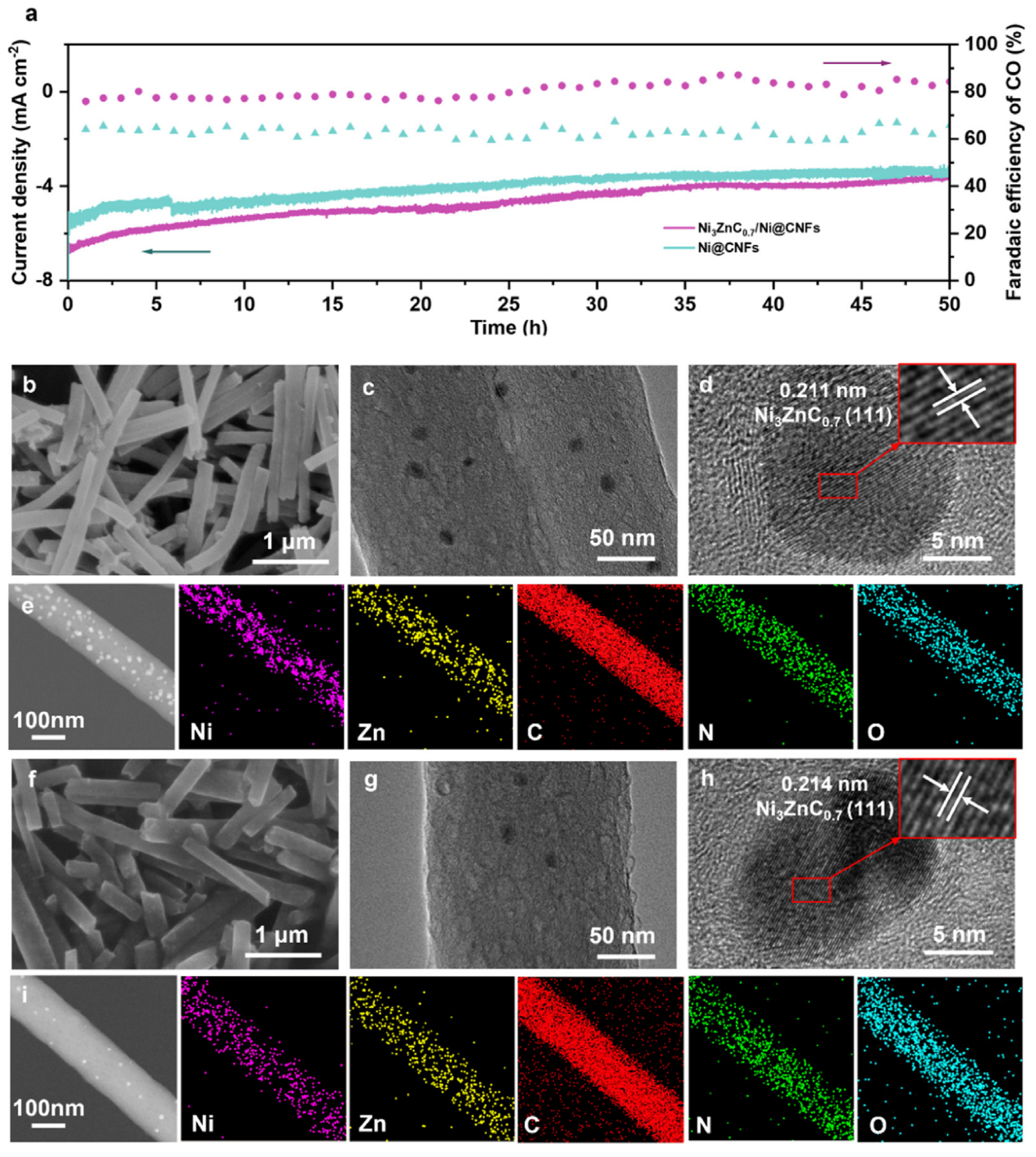

Fig. 4. a) Long-term stability of $Ni_3ZnC_{0.7}$/Ni@CNFs and Ni@CNFs at −0.86 V versus RHE. b) SEM image and c) TEM image of $Ni_3ZnC_{0.7}$/Ni@CNFs. d) High-resolution TEM and inverse fast fourier transformation of $Ni_3ZnC_{0.7}$/Ni@CNFs in the specific region of high-resolution TEM. e) TEM-EDS mapping results of $Ni_3ZnC_{0.7}$/Ni@CNFs. f) SEM image and g) TEM image of $Ni_3ZnC_{0.7}$/Ni@CNFs after 50 h of long-term stability. d) High-resolution TEM and inverse fast fourier transformation of $Ni_3ZnC_{0.7}$/Ni@CNFs after a 50-h stability test in the specific region of high-resolution TEM. e) TEM-EDS mapping results of $Ni_3ZnC_{0.7}$/Ni@CNFs after 50-h stability test.

The CO_2 must first dissolve in the catholyte and then be reduced to CO in the H-cell, which greatly limits the reaction rate of CO_2RR [64]. In contrast, the MEA reactor overcomes the mass transfer limitations of H-cell systems by facilitating direct gas-phase CO_2 delivery to the catalyst layer, while its compact architecture with closely spaced electrodes separated by thin ion-conducting membranes significantly reduces ohmic resistance and enhances charge transfer efficiency. Therefore, the MEA set-up as shown in Fig. 3f is attributed to the best candidate to overcome the above problem and boost the CO_2RR at the ampere level. The active area of the electrode is 2 × 2 cm^2. It is evident that the current density of $Ni_3ZnC_{0.7}$/Ni@CNFs rapidly increases when the applied cell voltage exceeds −3.0 V. When the applied cell voltage is −3.9 V, the total current density of the reactor reaches around 200 mA cm^{-2} in Fig. 3g, indicating that the $Ni_3ZnC_{0.7}$/Ni@CNFs exhibits high CO_2 electroreduction activity in the MEA cell. The FE_{CO} of $Ni_3ZnC_{0.7}$/Ni@CNFs increases from 80.1% to 90.1% with the applied potential from −2.4 to 3 V in Fig. 3h. Even with the applied cell voltage of −3.9 V, the FE_{CO} can still maintain 70.0%.

The long-term stability of electrocatalysts is crucial for practical applications. Stability tests, as shown in Fig. 4a, demonstrate that $Ni_3ZnC_{0.7}$/Ni@CNFs maintain a FE_{CO} of approximately 90% at −0.86 V versus RHE, with a current density of 4 mA cm^{-2} during 50 h of electrolysis. Although Ni@CNFs also exhibit good stability over the 50 h electrolysis period, both their current density and FE_{CO} are lower than those of $Ni_3ZnC_{0.7}$@CNFs. To elucidate the mechanism underlying this stability, pre- and post–experiment analyses of $Ni_3ZnC_{0.7}$/Ni@CNFs were conducted using TEM. The $Ni_3ZnC_{0.7}$/Ni@CNFs, mixed with a Nafion binder and air-sprayed onto hydrophobic carbon paper, display a well-defined fibrous structure with diameters ranging from 80 to 120 nm, as shown in Fig. 4b. This fibrous structure is well preserved after 20 and 50 h of electrolysis, as depicted in Fig. S16. However, TEM images of $Ni_3ZnC_{0.7}$/Ni@CNFs reveal that the surface of the carbon fibers is characterized by numerous bumps, hollows, and pores smaller than 3 nm, as shown in Fig. 4c. This observation is consistent with CO_2 adsorption–desorption results, indicating a high density of micropores and mesopores in $Ni_3ZnC_{0.7}$/Ni@CNFs. Ni/$Ni_3ZnC_{0.7}$ nanoparticles, approximately 10 nm in size, are uniformly distributed on the surface of the carbon fibers. The high-resolution TEM (HRTEM) image of $Ni_3ZnC_{0.7}$/Ni@CNFs in Fig. 4d shows a lattice spacing of 0.211 nm, corresponding to the (111) planes of $Ni_3ZnC_{0.7}$ (PDF #28-0713), which exhibits the highest intensity in the XRD patterns (Fig. 1b). Furthermore, energy-dispersive X-ray spectroscopy (EDS) mapping in Fig. 4e reveals that nitrogen and carbon elements are uniformly distributed within the carbon nanofibers, while nickel and zinc overlap evenly, consistent with the presence of nanoparticles. The morphology of $Ni_3ZnC_{0.7}$/Ni@CNFs remains largely unchanged after 50 h of electrolysis, as shown in Fig. 4f. The primary difference observed in $Ni_3ZnC_{0.7}$/Ni@CNFs after 50 h of electrolysis is a reduction in the number of Ni/$Ni_3ZnC_{0.7}$ nanoparticles, as seen in Fig. 4g, compared to the pristine $Ni_3ZnC_{0.7}$/Ni@CNFs in Fig. 4c. This reduction is corroborated by a decrease in the contents of Ni and Zn after CO_2 electrolysis, as shown in Fig. S17. EIS analysis revealed notable increases in R_S, R_{CP}, and R_{CT} values following prolonged CO_2 electrolysis, as shown in Fig. S18 and Table S4. The elevated R_S suggests electrolyte decomposition or ionic species depletion during operation, while the increased R_{CP} and R_{CT} reflect impaired charge transport within the catalyst matrix and diminished charge transfer at the catalyst–electrolyte interface, respectively. These observations correlate directly with the precipitation and loss of Ni and Zn active sites, as confirmed by TEM imaging showing reduced metal particle (Fig. 4h and i) and elemental mapping demonstrating decreased Ni and Zn content (Fig. S17). However, no differences are observed in the HRTEM images in Fig. 4h and the EDS mapping images in Fig. 4i, indicating that the crystal structure of $Ni_3ZnC_{0.7}$/Ni@CNFs remains unchanged after 50 h of electrolysis. Consequently, the FE_{CO} remains at a high level (~90%) during the long-term stability test.

5. Conclusions

In summary, a novel $Ni_3ZnC_{0.7}$/Ni heterostructure encapsulated in porous N-doped carbon nanofibers was successfully developed by an electrospinning strategy, which is an excellent catalyst for CO_2 reduction. The strategic incorporation of Zn enhances the performance of the catalyst by optimizing the adsorption of reaction intermediates and facilitating efficient electron transfer. Experimental results revealed that $Ni_3ZnC_{0.7}$/Ni@CNFs exhibited a notable FE_{CO} of nearly 90% and superior long-term stability for 50 h of continuous electrolysis at −0.86 V versus RHE in an H-cell. In a MEA setup, the $Ni_3ZnC_{0.7}$/Ni@CNFs catalyst achieved a FE_{CO} of 91.7% at a cell voltage of −3 V and a current density of 200 mA cm^{-2} at −3.9 V. Therefore, the development of $Ni_3ZnC_{0.7}$/Ni@CNFs with bimetallic heterogeneous by an electrospinning strategy provides a facile method for designing high-efficiency CO_2 reduction reaction electrocatalysts and further reveals the promising perspective of bimetallic carbides for CO_2 reduction reaction in the future.

CRediT authorship contribution statement

Ge Bai: Writing − original draft, Methodology, Data curation, Conceptualization. **Min Wang:** Investigation, Data curation. **Luwei Peng:** Data curation, Writing − review & editing. **Lulu Li:** Methodology, Investigation. **Yadan Yu:** Resources, Investigation. **Wenyi Li:** Resources, Investigation. **Nianjun Yang:** Visualization, Investigation. **Daniil I. Kolokolove:** Visualization, Data curation. **Jinli Qiao:** Writing − review & editing, Funding acquisition.

Declaration of competing interest

The author Jinli Qiao is an Editorial Board Member for Green Energy & Environment and was not involved in the editorial review or the decision to publish this article. The other authors declare that they have no known competing financial interests or personal relationships that could have appeared to influence the work reported in this paper.

Acknowledgment

The authors thank the financial support from the Natural Science Foundation of Yancheng (YCBK2024004), the Basic Research Program of Jiangsu (BK20251089) and the “Scientific and Technical Innovation Action Plan” Basic Research Field of Shanghai Science and Technology Committee (19JC1410500).

Appendix A. Supplementary data

Supplementary data to this article can be found online at https://doi.org/10.1016/j.gee.2025.04.010.

References

[1] P. Li, J. Bi, J. Liu, Q. Zhu, C. Chen, X. Sun, J. Zhang, B. Han, Nat. Commun. 13 (2022) 1965.
[2] S.-L. Zhou, Y. Dai, Q. Song, L. Lu, X. Yu, Inorg. Chem. 63 (2024) 24601–24609.
[3] S. Huang, Z. Fang, C. Lu, J. Zhang, J. Sun, H. Ji, J. Zhu, X. Zhuang, J. Colloid Interface Sci. 675 (2024) 683–688.
[4] H. Yang, Q. Lin, C. Zhang, X. Yu, Z. Cheng, G. Li, Q. Hu, X. Ren, Q. Zhang, J. Liu, C. He, Nat. Commun. 11 (2020) 593.
[5] Z. Zhao, C. Tan, P. Sun, F. Li, X. Wang, J. Mater. Chem. A 12 (2024) 21716–21722.
[6] H. Zhang, S. Zeng, C. Jiang, K. Peng, J. Feng, L. Yuan, X. Li, F. Xu, X. Zhang, ChemCatChem 16 (2024) e202400045.
[7] P. Chen, Y.-R. Wang, H. Shui, L.-P. Tang, S.-H. Wu, F.-C. Shen, Y.-Q. Lan, Inorg. Chem. 63 (2024) 22903–22911.
[8] K.-L. Bi, B.-H. Xu, W.-L. Ding, L.-J. Han, L. Ji, Green Energy Environ. 8 (2023) 296–307.
[9] J. Jiang, J. Lian, Z. Xu, Y. Wang, Y. Dong, J. Yan, D. Li, S. Liu, Adv. Funct. Mater. (2025) 2420881.
[10] L. Peng, C. Chen, R. He, N. Xu, J. Qiao, Z. Lin, Y. Zhu, H. Huang, EcoMat 4 (2022) e12260.
[11] L. Peng, Y. Wang, I. Masood, B. Zhou, Y. Wang, J. Lin, J. Qiao, F.-Y. Zhang, Appl. Catal. B Environ. 264 (2020) 118447.
[12] T. Dong, H. Li, Z. Wang, Y. Geng, R. Chang, X. Tian, J. Lai, S. Feng, L. Wang, Nano Res. 17 (2024) 5817–5825.
[13] G. Wang, F. Wang, P. Deng, J. Li, C. Wang, Y. Hua, Y. Shen, X. Tian, Mater. Rep. Energy 3 (2023) 100181.
[14] Y. Zang, T. Liu, P. Wei, H. Li, Q. Wang, G. Wang, X. Bao, Angew. Chem. Int. Ed. 61 (2022) e202209629.
[15] Y. Sha, J. Zhang, X. Cheng, M. Xu, Z. Su, Y. Wang, J. Hu, B. Han, L. Zheng, Angew. Chem. Int. Ed. 61 (2022) e202200039.
[16] Z. Wan, A. Kuchkaev, D. Yakhvarov, X. Kang, J. Electrochem. 30 (1) (2024) 1–10.
[17] D. Bagchi, M. Riyaz, J. Raj, S. Roy, A.K. Singh, A. Cherevotan, C.P. Vinod, S.C. Peter, Chem. Mater. 36 (2024) 3464–3476.
[18] R. Zhang, J. Zhang, S. Wang, Z. Tan, Y. Yang, Y. Song, M. Li, Y. Zhao, H. Wang, B. Han, R. Duan, Angew. Chem. Int. Ed. 63 (2024) e202405733.
[19] X. Li, S. Zeng, A. Wang, G. Li, L. Yuan, K. Peng, C. Jiang, H. Zhang, X. Zhang, S. Zhang, Chem. Eng. Sci. 292 (2024) 119961.
[20] S. Wu, Y. Zhang, D. Ping, Y. Li, W. Li, S. Liu, D. Wu, S. Wang, X. Yang, G. Han, D. Guo, S. Fang, Carbon 228 (2024) 119428.
[21] Z. Fang, Y. Zhai, W. Guo, Z. Sun, L. Jiao, Z. Zhu, X. Lu, J. Tang, Chem. Commun. 60 (2024) 3575–3578.
[22] Z. Xu, J. Sun, Q. Wang, Int. J. Hydrogen Energy 60 (2024) 976–984.
[23] W. Luo, J. Zhang, M. Li, A. Züttel, ACS Catal. 9 (2019) 3783–3791.
[24] Q. He, D. Liu, J.H. Lee, Y. Liu, Z. Xie, S. Hwang, S. Kattel, L. Song, J.G. Chen, Angew. Chem. Int. Ed. 59 (2020) 3033–3037.
[25] B. Chang, Z. Min, N. Liu, N. Wang, M. Fan, J. Fan, J. Wang, Green Energy Environ. 9 (2024) 1085–1100.
[26] Z. Wei, M. Cao, R. Cao, J. Electrochem. 29 (2023) 2215008.
[27] L. Peng, Y. Wang, Y. Wang, N. Xu, W. Lou, P. Liu, D. Cai, H. Huang, J. Qiao, Appl. Catal. B Environ. 288 (2021) 120003.
[28] Y. Li, Z. He, F. Wu, S. Wang, Y. Cheng, S. Jiang, Mater. Rep. Energy 3 (2023) 100197.
[29] H. Yang, H. Chuai, Q. Meng, M. Wang, S. Zhang, X. Ma, Mater. Rep. Energy 3 (2023) 100174.
[30] S. Gao, H. Li, Z. Lu, S. Meng, X. Zhao, X. Wang, X. Liu, G. Hu, Carbon Energy 7 (2024) e637.
[31] P. Liu, Y. Liu, K. Wang, S. Shi, M. Jin, J. Liu, T. Qin, Q. Liu, X. Liu, J. He, Nano Res. 17 (2024) 7957–7966.
[32] Z. Kang, M. Zhang, Y. Wang, P. Yue, J. Li, X. Zhu, Q. Fu, Q. Liao, Catal. Today 450 (2025) 115208.
[33] X. Shao, Z. Bian, B. Li, F. Zhan, X. Cheng, Y. Shen, Z. Li, Q. Zhou, R. Cai, C. Feng, Sep. Purif. Technol. 359 (2025) 130576.
[34] F. Mao, P.F. Liu, P. Yang, J. Gu, H.G. Yang, ACS Appl. Nano Mater. 3 (2020) 8581–8585.
[35] Y. Wang, Q. Zhang, C. Wang, Ayeza, Y. Zhang, C. Hu, Chem. Asian J. 20 (2024) e202401250.
[36] J. Sun, H. Zhou, J. Xu, M. Wang, X. Liu, X. Huang, Y. Wang, S. Bai, Z. Huang, Appl. Catal. B Environ. 358 (2024) 124396.
[37] K. Lian, J. Ding, J. Zhang, Q. Zhang, Y. Liu, G. Hu, J. He, X. Liu, J. Mater. Chem. A 13 (2025) 2010–2018.
[38] Q. Pan, Y. Chen, H. Li, G. Ma, S. Jiang, X. Cui, L. Zhang, Y. Bao, T. Ma, J. Mater. Chem. A 12 (2024) 20035–20044.
[39] Y. Zhao, X. Yu, Z. Wu, Y. Li, W. Wang, L. Feng, Z. Sui, Q. Chen, Adv. Sustain. Syst. 8 (2024) 2400284.
[40] L.-Q. Liu, S. Guan, Z.-N. Chen, S.-Y. Sun, C.-Y. Lan, J.-Z. Wang, P.-F. Yin, J. Yang, H. Liu, X.-W. Du, C. Dong, Ind. Eng. Chem. Res. 63 (2024) 8133–8141.
[41] X. Rong, H.J. Wang, X.L. Lu, R. Si, T.B. Lu, Angew. Chem. Int. Ed. 59 (2019) 1961–1965.
[42] L. Qiu, S. Shen, C. Ma, C. Lv, X. Guo, H. Jiang, Z. Liu, W. Qiao, L. Ling, J. Wang, Chem. Eng. J. 440 (2022) 135956.
[43] Q. Pang, X. Fan, K. Sun, K. Xiang, B. Li, S. Zhao, Y.D. Kim, Q. Liu, Z. Liu, Z. Peng, Energy Environ. Mater. 7 (2024) e12731.
[44] W. Ma, J. Yao, F. Xie, X. Wang, H. Wan, X. Shen, L. Zhang, M. Jiao, Z. Zhou, Green Energy Environ. 10 (2025) 109–131.
[45] Y. Li, B. Wei, M. Zhu, J. Chen, Q. Jiang, B. Yang, Y. Hou, L. Lei, Z. Li, R. Zhang, Y. Lu, Adv. Mater. 33 (2021) 2102212.
[46] K. Mou, Z. Chen, X. Zhang, M. Jiao, X. Zhang, X. Ge, W. Zhang, L. Liu, Small 15 (2019) 1903668.
[47] M. Liang, Y. Liu, H. Huang, L. Diao, J. Mu, Z. Miao, J. Zhou, S. Zhuo, Chem. Eng. J. 450 (2022) 137962.
[48] Y. Zhang, H. Jiang, A. Kumar, H. Zhang, Z. Li, T. Xu, Y. Pan, Y. Wang, Z. Liu, G. Zhang, Z. Yan, Carbon Energy 5 (2023) e341.
[49] Y. Tuo, Q. Lu, W. Liu, M. Wang, Y. Zhou, X. Feng, M. Wu, D. Chen, J. Zhang, Small 20 (2023) 2306945.
[50] J. Li, Z. Cao, X. Zhang, L. Gao, X. Liu, L. Chen, Y. Zhang, Q. Zhang, P. Zhang, T. Liu, Mol. Catal. 558 (2024) 114050.
[51] J. Wang, Z. Li, Z. Zhu, J. Jiang, Y. Li, J. Chen, X. Niu, J.S. Chen, R. Wu, J. Energy Chem. 75 (2022) 1–7.
[52] L. Liao, C. Jia, S. Wu, S. Yu, Z. Wen, S. Ci, Nanoscale 16 (2024) 8119–8131.
[53] X. Wei, S. Xiao, R. Wu, Z. Zhu, L. Zhao, Z. Li, J. Wang, J.S. Chen, Z. Wei, Appl. Catal. B Environ. 302 (2022) 120861.
[54] Z. He, P. Wei, T. Xu, Z. Guo, J. Han, T. Akasaka, K. Guo, X. Lu, Nanoscale 14 (2022) 473–481.
[55] Y. Chang, J. Chen, J. Jia, X. Hu, H. Yang, M. Jia, Z. Wen, Appl. Catal. B Environ. 284 (2021) 119721.
[56] C. Ding, Z. Liu, S. Pan, C. Zhao, Z. Wang, B. Gao, Q. Li, Chem. Eng. J. 460 (2023) 141729.

[57] P. Zhang, H. Chen, L. Chen, Y. Xiong, Z. Sun, H. Yang, Y. Fu, Y. Zhang, T. Liao, F. Li, Chin. J. Catal. 45 (2023) 152–161.
[58] T. Lu, N. Xu, L. Guo, B. Zhou, L. Dai, W. Yang, G. Liu, J.K. Lee, J. Qiao, Adv. Fiber Mater. 6 (2024) 1108–1121.
[59] R. Boppella, Y. Kim, K.A. Joshi Reddy, I. Song, Y. Eom, E. Sim, T.K. Kim, Appl. Catal. B Environ. 345 (2024) 123699.
[60] L. Feng, H. Yin, L. Dai, Y. Zhang, C. Fu, L. Cao, Y. Li, D. Zhao, Y. Xie, J. Huang, Inorg. Chem. Front. 10 (2023) 6294–6302.
[61] L. Jiao, X. Li, W. Wei, S.-H. Zhou, S.-G. Han, D.-D. Ma, Y. Mao, Q. Xu, X.-T. Wu, Q.-L. Zhu, Appl. Catal. B Environ. 330 (2023) 122638.
[62] Z. Lu, B. Wang, Y. Hu, W. Liu, Y. Zhao, R. Yang, Z. Li, J. Luo, B. Chi, Z. Jiang, M. Li, S. Mu, S. Liao, J. Zhang, X. Sun, Angew. Chem. 131 (2019) 2648–2652.
[63] S. Fan, H. Cheng, M. Feng, X. Wu, Z. Fan, D. Pan, G. He, Chin. J. Chem. Eng. 39 (2021) 144–153.
[64] P. Liu, L. Peng, R. He, L. Li, J. Qiao, J. Electrochem. 28 (1) (2022) 1–9.